SNOW MAPPING USING MULTI-TEMPORAL METEOSAT-8 DATA

Martijn de Ruyter de Wildt [1], Gabriela Seiz [2] and Armin Grün [1]

1. ETH Zurich, Institute of Geodesy and Photogrammetry, Zurich, Switzerland; ruyter(at)geod.baug.ethz.ch
2. MeteoSwiss, Zurich, Switzerland

ABSTRACT

Meteosat-8 is the first geostationary satellite that possesses channels at all bandwidths that are of use for snow mapping. It therefore offers new possibilities for multi-temporal snow mapping as well as for snow mapping at short time intervals, which is for example required for numerical weather prediction models. The spectral capabilities of Meteosat-8 allow an optimal spectral separation of clouds and surface snow cover, but there always may be clouds with spectral characteristics similar to those of snow. In this study, we propose a classification technique that uses temporal information, in addition to spectral information, to detect these clouds. This technique is based on the temporal differences which often exist between subsequent values of a cloud-covered pixel. The inclusion of temporal information in the classification process improves the classification of images from a three-day test period in March 2004.

Keywords: Snow, MSG, SEVIRI, multi-temporal.

INTRODUCTION

For the numerical simulation of atmospheric processes in Numerical Weather Prediction (NWP) models, it is important to correctly model the energy exchange between the ground and the atmosphere. All the components of the process (momentum flux, short wave upward radiation, long wave upward radiation, latent heat flux and sensible heat flux) are significantly modified when snow covers the ground. It is therefore important to correctly prescribe surface snow cover at NWP model initialisation times. But existing snow input data are mostly not accurate enough: data from conventional climate stations are too sparse to fulfil the requirements of the most recent operational high resolution models, whereas, until recently, only some polar orbiting (low frequency) sensors possessed the necessary spectral channels for snow/cloud separation. The new generation of European geostationary satellites, starting with Meteosat-8, helps to close this gap.

Several satellite sensors that have been used for mapping surface snow cover are listed in Figure 1. NOAA AVHRR combines a repeat time of several hours with a spectral resolution of 1 km at nadir, which has made it a popular sensor for snow mapping (e.g. 1,2,3,4). Originally, the AVHRR instrument did not have a 1.6 µm channel, which is important for separating snow and clouds, but recent AVHRR sensors (since NOAA-15, launched in 1999) are equipped with such a channel. Another sensor that is suitable for snow mapping is MODIS, on board of NASA's Terra and Aqua satellites. It has 36 narrow spectral bands and can be used to produce daily snow maps with a spatial resolution of 500 m (5). Other sensors with which snow cover has been mapped are Landsat TM (e.g. 6) and Terra/Aqua ASTER (7,8), but these have high spatial resolutions and long repeat times and are therefore not suitable for snow mapping on a daily basis. The same applies to MERIS, on board of ESA's Envisat, which will also be used for mapping snow cover (9).

Geostationary satellites have a much higher temporal resolution than polar orbiting satellites, which can be used to reduce the obscuration of the surface by clouds and to update the surface snow cover on a more frequent basis. The spatial resolution of geostationary satellites is rather low, typically several km, but this is still higher than that of currently operational NWP models. Nevertheless, the predecessors of Meteosat-8 have not been used for snow mapping, because they have only 2 channels (visible and infrared) that detect surface radiation. The only geostationary satellites that, until recently, could be used for detecting surface snow cover were the Geostationary Opera-

tional Environmental Satellites (GOES) (10,11). The Imager instrument on board of these satellites has three channels that are of use for snow mapping (at 0.64, 3.9 and 10.7 µm), which is less than most polar orbiting sensors possess, but the high frequency aids the classification considerably.

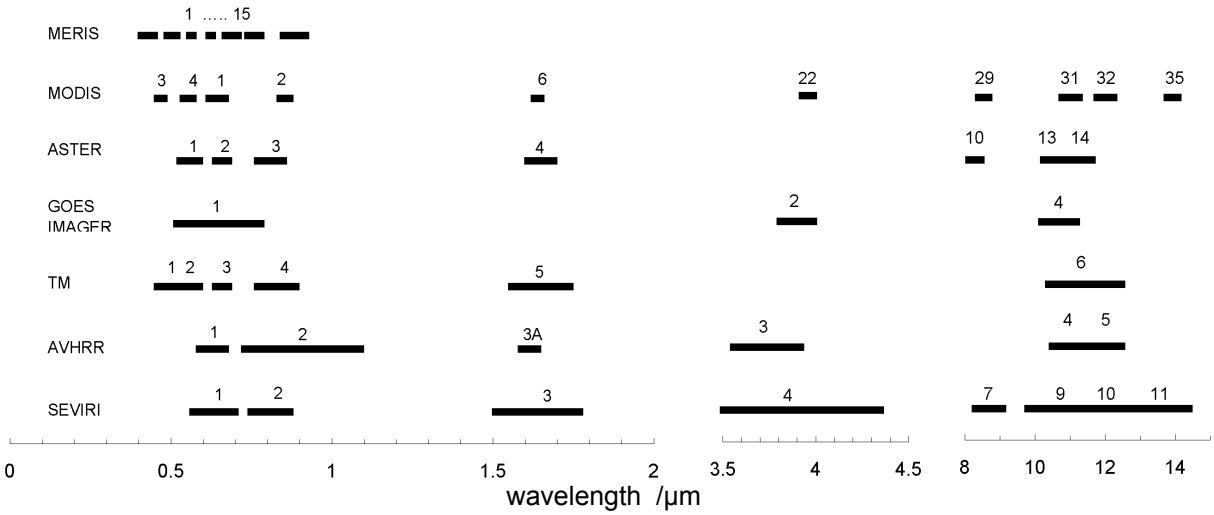

Figure 1: A comparison of the spectral channels of several satellite sensors that have been used for snow mapping (in random order). Only channels that are relevant for snow mapping are shown.

In 2002, the first Meteosat Second Generation satellite (MSG-1) was launched by the European Organisation for the Exploitation of Meteorological Satellites (EUMETSAT). This satellite, now known as Meteosat-8, carries the Spinning Enhanced Visible and Infrared Imager (SEVIRI), which is the first geostationary instrument that measures at all bandwidths that are of use for snow mapping. Furthermore, it has a temporal resolution of 15 minutes, whereas its predecessors on board of the previous Meteosat satellites have a temporal resolution of 30 minutes. It therefore allows a good separation between snow and clouds and makes it possible to monitor surface snow cover on a very regular basis. This study presents the first results of a EUMETSAT fellowship that aims at developing an automated snow mapping algorithm for Meteosat-8 data. This algorithm is intended for delivering real-time snow cover data to the operational mesoscale NWP model of MeteoSwiss, the Alpine Model (aLMo). It should therefore be applicable over alpine terrain, and in this respect it differs from two other snow mapping algorithms for Meteosat-8 data. These algorithms are being developed by two EUMETSAT Satellite Application Facilities (SAFs): the Nowcasting SAF (12) and the Land Surface Analysis SAF (13). An additional important aspect of the project is to investigate possibilities for using the multitemporal information content of Meteosat-8 data for snow mapping.

Spectral classification, which is used in all of the above-mentioned applications, generally gives good results, but problems arise for clouds with spectral properties similar to those of surface snow. Such clouds are optically thick, have partially or entirely frozen tops and have (nearly) the same temperature as the surface. A way to avoid confusing these clouds with snow is to analyse the context of a pixel. Several authors have used pattern recognition techniques to classify polar satellite images (e.g. 14,15), but these techniques are used for classifying blocks of pixels, and not individual pixels. If they were applied to Meteosat-8 data, the resolution of the classification result would be too low for use in mesoscale NWP models. Also, these methods detect the spatial variability that clouds often display, and are therefore best suited for cloud mapping over homogeneous regions and for distinguishing between different cloud types. They are less suitable to detect clouds over land surfaces with strong variation, such as snow-covered mountain chains and regions with patchy snow cover. An analysis of the temporal context of clouds therefore seems more usable. Irrespective of their spectral signature, clouds often display a much more dynamic behaviour than the earth's surface, and the high temporal resolution of Meteosat-8 allows us to monitor this behaviour at very short time scales. In this study we describe a method that uses temporal information in addition to spectral information to mask clouds over snow-covered regions.

DATA

Meteosat-8 is currently situated at 3.4° western longitude at an altitude of 36,000 km. SEVIRI continuously monitors the entire earth disk at a frequency of 15 minutes and has 12 spectral channels, 8 of which can be used for monitoring the surface (Table 1). Channel 12 is a high resolution visible (hrv) channel, which has a resolution of 1 km at the sub-satellite point (1.5 – 2 km over Central Europe). All of the other channels have a spatial resolution of 3 km at the sub-satellite point (5 – 6 km over Central Europe). The area of interest is central Europe, which is the model domain of aLMo.

Table 1. The twelve channels of the SEVIRI instrument on board of Meteosat-8.

Channel	Spectral band /µm			Description
	centre	min.	max.	
1	0.635	0.56	0.71	visual
2	0.81	0.74	0.88	visual
3	1.64	1.50	1.78	near infrared
4	3.90	3.48	4.36	infrared
5	6.25	5.35	7.15	infrared (water vapour absorption)
6	7.35	6.85	7.85	infrared (water vapour absorption)
7	8.70	8.30	9.1	infrared
8	9.66	9.38	9.94	infrared (ozone absorption)
9	10.80	9.80	11.80	infrared
10	12.00	11.00	13.00	infrared
11	13.40	12.40	14.40	infrared (CO_2 absorption)
12	0.75	0.60	0.90	high resolution visual broadband (hrv)

For testing and validation we selected a three-day period in March 2004. Especially at this time of the year, the snow cover of the pre-alpine regions in Switzerland can be highly variable. In such circumstances it is difficult for NWP models to model the snow cover accurately, which makes satellite-derived snow cover especially useful. During the selected period, March 8th till March 10th, all mountainous regions of Europe were covered with snow as well as large parts of Central, Eastern and Northern Europe. The weather was variable, with low pressure activity over Central Europe and the Mediterranean. Clouds, some of them containing ice particles, bare land and snow-covered land were all well represented over Europe, making this period suitable for testing a snow mapping algorithm. All 288 images acquired during these three days are available, but we only use the day time images for snow mapping.

The Meteosat-8 data that we use are provided in Level 1.5 Native Format. These consist of raw satellite counts, which need to be calibrated and converted into reflectances (r) and brightness temperatures (BT). For extraction, calibration and geo-location of the data we use the SEVIRI Pre-processing Toolbox version 2.2 (16), which we incorporated into our processing chain. Calibration constants and methods for conversion of the radiances into reflectances and brightness temperatures are described in (17) and (18). We also applied a sea mask to the data, which is based on the SRTM30 Digital Elevation Model (DEM) of NASA and the United States Geological Survey. This global DEM has a horizontal resolution of 1 km and was resampled to the Meteosat-8 grid with bicubic interpolation.

METHODS

As a basis for classification we use several spectral threshold tests that are in common use. These tests are used to designate each pixel to one of three classes: cloud, snow or bare land. All pixels that are spectrally classified as snow will be subjected to a temporal test, in order to detect any

clouds that were erroneously classified as snow. The overall classification scheme is shown in Figure 2.

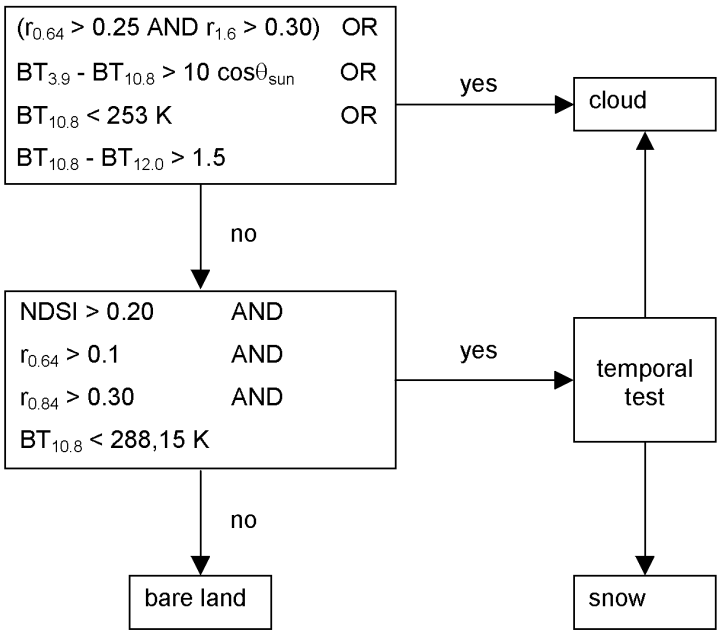

Figure 2: Flowchart for classification.

Spectral classification

Existing algorithms for spectral classification of snow use several satellites and sensors. These sensors have channels in the same spectral regions, although the exact bandwidths vary (Figure 1). For some of the spectral threshold tests we therefore empirically adapted the thresholds. To avoid problems that are caused by a low solar zenith angle (sza), pixels with a sza above 75° are discarded. A pixel is masked as cloud if at least one of the following threshold tests is passed:

- $r_{0.64}$ > 0.25 and $r_{1.6}$ > 0.30 (e.g. 6,19). The 0.64 µm test separates bare ground from snow and clouds. Many clouds can be distinguished from snow in the 1.6 µm channel, which is sensitive to the phase of the clouds (e.g. (6)). However, this channel cannot separate some ice clouds from snow.
- $BT_{3.9}$ - $BT_{10.8}$ > 10 cosθ_s, where θ_s is the solar zenith angle. This thermal difference has been used by several authors (e.g. 3,4,19). Unlike the earth's surface, water clouds emit less radiation at 3.8 µm than at 10.8 µm, and hence display a brightness temperature difference between these channels (20). Cirrus clouds also display a high $BT_{3.9}$ - $BT_{10.8}$, because they transmit more relatively warm surface radiation in the 3.8 µm channel than in the 10.8 µm channel (20). Optically thick ice clouds do not transmit surface radiation and display the same small difference as the surface. The threshold depends on the solar zenith angle (12), because the SEVIRI 3.9 µm channel not only detects terrestrial radiation, but also a small amount of solar radiation.
- $BT_{10.8}$ < $BT_{10.8,min}$ (1,11). This test separates very cold clouds from snow. The optimal threshold value for this test would ideally be the surface temperature, but as this parameter is not known, we use a fixed threshold, $BT_{10.8,min}$ = 253 - 0.0063z. Here, z is the surface altitude (in metres) and 0.0063 the atmospheric lapse rate.
- $BT_{10.8}$ - $BT_{12.0}$ > 1.5 (8,12). Like $BT_{3.9}$ - $BT_{10.8}$, this split window thermal difference is mostly higher for clouds (especially cirrus) than for clear skies.

Pixels that are not classified as cloudy in this way are checked for the presence of snow by a second suite of tests. A cloud-free pixel is classified as snow if all of the following conditions are fulfilled:

- *NDSI* > 0.2, where *NDSI* stands for Normalised Differential Snow Index (6,21). This index equals ($r_{0.64}$ - $r_{1.6}$) / ($r_{0.64}$+ $r_{1.6}$) and enlarges the contrast between snow and bare ground, as snow has a higher $r_{0.64}$ and a lower $r_{1.6}$ than snow-free land.
- $r_{0.64}$ > 0.1. This criterion ensures that very dark surfaces, which can cause the denominator of the *NDSI* to be very small, are not classified as snow (5).
- $r_{0.81}$ > 0.3. Without this criterion some pixels at the border of land and sea are mapped as snow, probably due to sub-pixel errors in geo-location.
- $BT_{10.8}$ < 288 K (4,5,11). The temperature of snow cannot rise above the freezing point, which is why an upper limit is set for $BT_{10.8}$. This upper limit is fairly high to account for rocks and tree-tops that may be present in snow-covered areas and that can raise the apparent brightness temperature substantially (11).

Temporal classification

As a basis for the quantification of the temporal behaviour of pixel values, we use the temporal difference between two successive values of a pixel. This difference is often larger for cloudy pixels than for clear pixels, although cloudy pixels that display high variation in one channel may display much less variation in other channels. An effective cloud mask can therefore be obtained by thresholding the temporal differences in each channel (or combination of channels) separately, and then stacking all single-channel cloud masks. We tested several classifiers that are based on the temporal difference. The simplest one is the absolute difference with the previous pixel value:

$$d_m = \left| I_{m,t} - I_{m,t-1} \right| \tag{1}$$

where m is the SEVIRI channel number, I the reflectance or the brightness temperature in this channel and t the time. The next pixel value can also be taken into account:

$$d_m = \left| I_{m,t} - I_{m,t-1} \right| + \left| I_{m,t+1} - I_{m,t} \right| \tag{2}$$

as well as the same information for the eight surrounding pixels:

$$d_m = \frac{\sum_{i=-1}^{1} \sum_{j=-1}^{1} \left(\left| I_{m,i,j,t} - I_{m,i,j,t-1} \right| + \left| I_{m,i,j,t+1} - I_{m,i,j,t} \right| \right)}{9} \tag{3}$$

where i and j are spatial indices in the x and y directions, respectively. Although this classifier considers the 8 surrounding pixels, it does not quantify spatial variability, and can therefore be regarded as a quasi three-dimensional classifier. The full three-dimensional variability (both spatial and temporal) can be quantified in a simple way with the three-dimensional standard deviation:

$$d_m = \sum_{i=-1}^{1} \sum_{j=-1}^{1} \sum_{t=-1}^{1} \mathrm{sqrt}\left(\frac{\left(I_{m,i,j,t} - \hat{I} \right)^2}{27} \right) \tag{4}$$

where $\hat{I}$ is the average reflectance or brightness temperature for the three-dimensional block of 27 pixels. Finally, we also computed the two-dimensional (only x and y) standard deviation:

$$d_m = \sum_{i=-1}^{1} \sum_{j=-1}^{1} \mathrm{sqrt}\left(\frac{\left(I_{m,i,j} - \hat{I} \right)^2}{9} \right) \tag{5}$$

Before each of these classifiers can be used, appropriate thresholds that differentiate between clear and cloudy pixels must be found. As explained above, we apply a threshold test to each channel separately, which is why we use a simple univariate minimum distance classification. A pixel is classified as ‘cloudy’, if the normalised Euclidean distance from the class ‘cloudy’ is smaller than the normalised Euclidean distance from the class ‘clear’ in at least one channel:

$$\frac{(d_m - \hat{d}_{m,cloudy})}{\sigma_{m,cloudy}} < \frac{(d_m - \hat{d}_{m,clear})}{\sigma_{m,clear}} \quad (6)$$

where $\hat{d}_m$ is the mean value and σ_m the standard deviation of d_m for the classes 'cloudy' and 'clear'. These classes are not known a priori (it is in fact the goal of this temporal classification to find them), but the spectral classification offers a good approximation. The spectral classification may contain some errors due to the confusion of clouds with snow, but this effect can be tempered by adding safety margins to the spectral thresholds. In order to define training areas for the temporal classification, we therefore perform a second spectral classification for each image, this time with adapted thresholds. The applied safety margins are ±0.02 for $r_{1.6}$ ±2 K for $BT_{3.9}$ - $BT_{10.8}$ and ±0.35 K for $BT_{10.8}$ - $BT_{12.0}$. After this second spectral classification, which results in an initial definition of clear and cloudy regions, the means and standard deviations of each d_m can be computed and for each pixel Eq. (6) can be evaluated.

We found that, in general, $\hat{d}_m$ and σ_m are fairly constant for successive images, but for images with low solar zenith angles they vary widely and are not very reliable. The possible cause for this seems to be the lower number of pixels in these images that can be used for training. For images with a low central solar zenith angles we therefore prescribe average values for $\hat{d}_m$ and σ_m, obtained from the images with high solar zenith angles.

The performance of each classifier can be quantified with the following divergence parameter (22):

$$D_m = \frac{\left| \hat{d}_{m,cloudy} - \hat{d}_{m,clear} \right|}{\sigma_{m,cloudy} + \sigma_{m,clear}} \quad (7)$$

which indicates the ability of feature m to separate the two classes. Values of D_m for the five classifiers are given in Table 2. They are computed for all eight SEVIRI channels that can detect surface radiation, including the hrv channel. The hrv channel has exactly nine pixels in each normal (low) resolution pixel, and we obtain a value of d_m for the low resolution pixels by simply adding all nine high resolution values. We computed the divergence for the eight usable channels and also for the two thermal differences that we use for spectral classification of clouds, $BT_{3.9}$ - $BT_{10.8}$ and $BT_{10.8}$ - $BT_{12.0}$. There are two other combinations of channels that are reported to distinguish between clouds and snow, but that we do not use for spectral classification: the *NDSI* (21) and $BT_{8.9}$ - $BT_{10.8}$ (8). We found that the temporal differences of the *NDSI* are not particularly useful for classification, in contrast to differences in $r_{0.64}$ - $r_{1.6}$, the numerator of this index. Hence, we computed the divergence also for $r_{0.64}$ - $r_{1.6}$ and for $BT_{8.9}$ - $BT_{10.8}$. Table 2 shows that, for all features, the divergence increases as more temporal information is used (from classifier 1 to classifier 3; also from classifier 5 to classifier 4). Classifier 3 performs best in separating clouds and snow and we will therefore use this classifier for temporal classification of the images.

As might have been expected, the highest divergence is found for the reflectance in the hrv channel, which detects the most detailed information. The other three solar channels, as well as the thermal difference $BT_{3.9}$ - $BT_{10.8}$, also display high divergences. The next best feature, $r_{0.64}$ - $r_{1.6}$, has a somewhat lower divergence, but we found that this feature still eliminates some clouds that are spectrally misclassified as snow. The same applies to the 3.9 µm channel. Inclusion of any of the remaining features does not alter the result significantly, so these are not used for temporal classification.

In sum, the temporal classification consists of the following steps:

- use spectral classification with adapted thresholds to obtain an initial definition of the classes 'cloudy' and 'clear';
- compute means and standard deviations of d_m for both classes and for each spectral feature m;

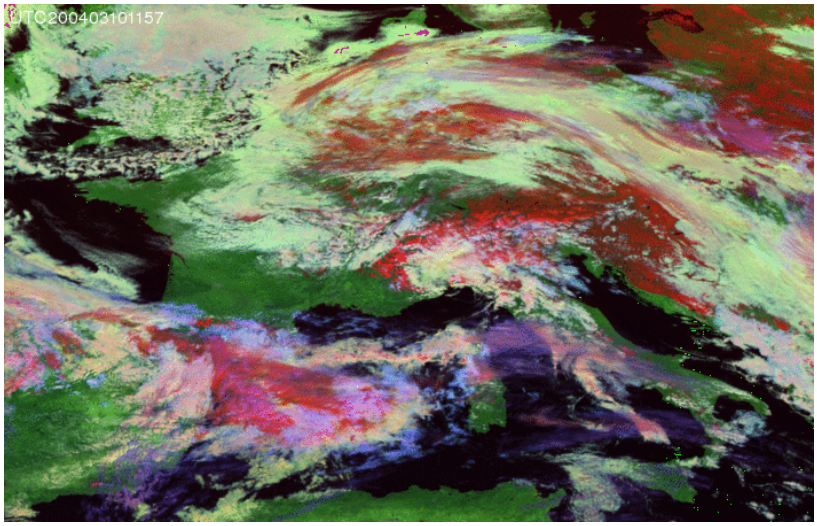

Figure 3: Meteosat-8 RGB image of central Europe, acquired on March 10th, 2004, starting scan time 11:45. It has been made from the 0.64 µm reflectance (red), the 1.6 µm reflectance (green) and the 3.9 - 10.8 µm brightness temperature difference (blue).

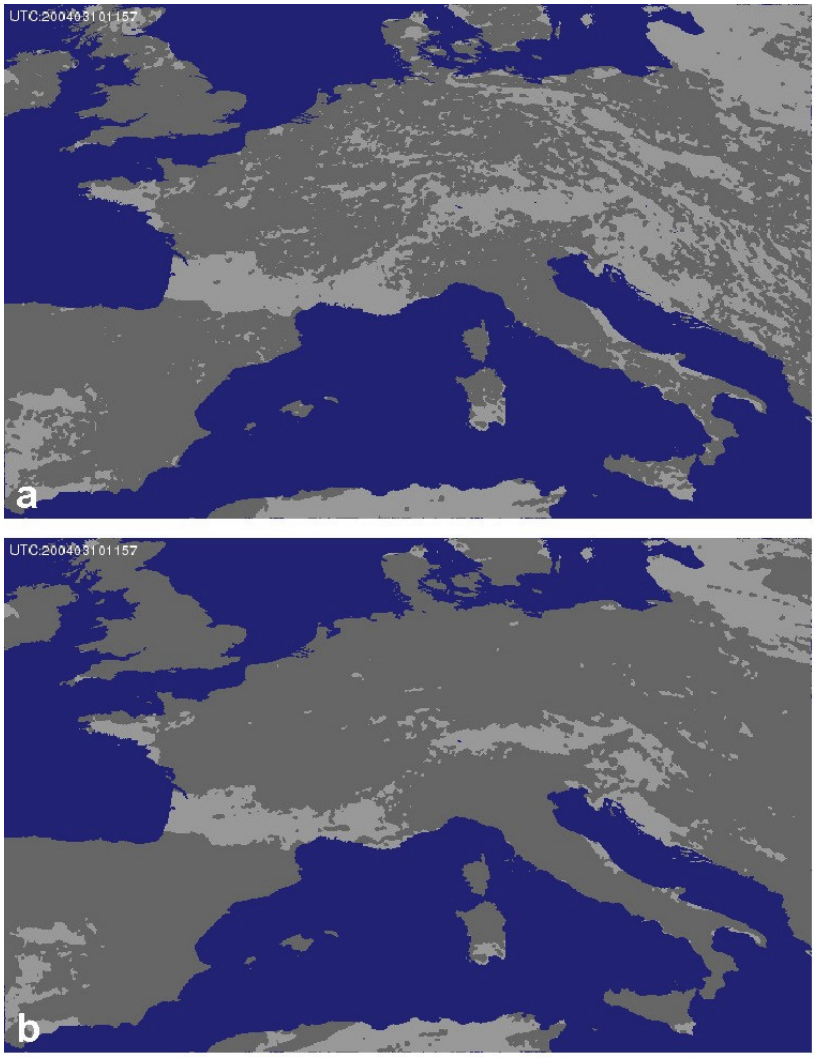

Figure 4: Temporal cloud mask for March 10th, 2004, starting scan time 11:45. (a) only for $r_{0.64}$ and without spatial consistency filtering and (b) for all used features $r_{0.64}$, $r_{0.81}$, $r_{1.6}$, $r_{0.64}$ - $r_{1.6}$, $BT_{3.9}$, $BT_{3.9}$ - $BT_{10.8}$ and r_{hrv}, with spatial consistency filtering. Light grey pixels are cloud-free, dark grey pixels are cloudy.

- for each pixel in the image and for each of the features $r_{0.64}$, $r_{0.81}$, $r_{1.6}$, $r_{0.64}$ - $r_{1.6}$, $BT_{3.9}$, $BT_{3.9}$ - $BT_{10.8}$ and r_{hrv}, compute the normalised Euclidean distance to the classes 'cloudy' and 'clear';
- label a snow pixel as 'cloudy' if for one or more of these features, the normalised Euclidean distance from the class 'cloudy' is smaller than the normalised Euclidean distance from the class 'clear'.

Some cloudy pixels that are not recognised by this temporal classification can be removed with a spatial consistency filter. This filter labels any non-clouded pixel that is surrounded by at least six cloudy pixels as cloudy.

Table 2. Divergence parameters for the separation of clear and cloudy pixels, given for 5 different classifiers that are applied to 12 spectral features. The numbers of the five classifiers correspond to Eqs. (1) to (5). Mean values are shown, calculated for all available images with a central solar zenith angle below 68°.

Feature	Classifier				
	1	2	3	4	5
$r_{0.64}$	0.49	0.60	0.70	0.43	0.31
$r_{0.81}$	0.50	0.61	0.72	0.40	0.27
$r_{1.6}$	0.48	0.58	0.69	0.48	0.37
$BT_{3.9}$	0.41	0.50	0.57	0.48	0.35
$BT_{8.7}$	0.37	0.46	0.51	0.47	0.42
$BT_{10.8}$	0.35	0.43	0.48	0.44	0.40
$BT_{12.0}$	0.33	0.41	0.45	0.40	0.37
$r_{0.64}$ - $r_{1.6}$	0.41	0.50	0.58	0.12	0.00
$BT_{3.9}$ - $BT_{10.8}$	0.47	0.59	0.69	0.65	0.54
$BT_{8.7}$ - $BT_{10.8}$	0.34	0.43	0.55	0.49	0.46
$BT_{10.8}$ - $BT_{12.0}$	0.31	0.38	0.54	0.55	0.52
r_{hrv}	0.61	0.72	0.75	0.52	0.32

Composite snow maps

All instantaneous snow maps that are obtained during a certain period can be combined into a composite snow map for this period. For this compositing, we use the technique of Hall et al. (5) as a basis, who label a pixel in the composite map as snow, if it is classified as snow in at least one of the individual satellite images. The high temporal resolution of Meteosat-8 allows us to extend the compositing procedure with a temporal consistency test: If a pixel is classified as snow in one image but not in the two neighbouring images, it is considered to be a cloud. This temporal consistency test helps to remove remaining misclassified cloudy pixels. Finally, we subject the composite snow map to a spatial consistency test that reclassifies any pixel that is entirely surrounded by another class.

RESULTS

For analysing the performance of the algorithm, we focus on March 10th, 2004. One of the images from this day is shown as an RGB composite in Figure 3. It is made from three spectral features that are important for snow mapping: the 0.64 µm reflectance (red), the 1.6 µm reflectance (green) and the 3.9 µm - 10.8 µm brightness temperature difference (blue). Most image classes are clearly discernible from each other in this RGB combination. Green pixels in this image correspond to non-cloudy areas without snow cover. These have a low visible reflectance, medium near-infrared reflectance and a low brightness temperature difference. Snow-covered areas are red: they have a high visual reflectance, a low near infrared reflectance and a low brightness temperature difference. Water clouds have high values in all three channels and appear in bright colours.

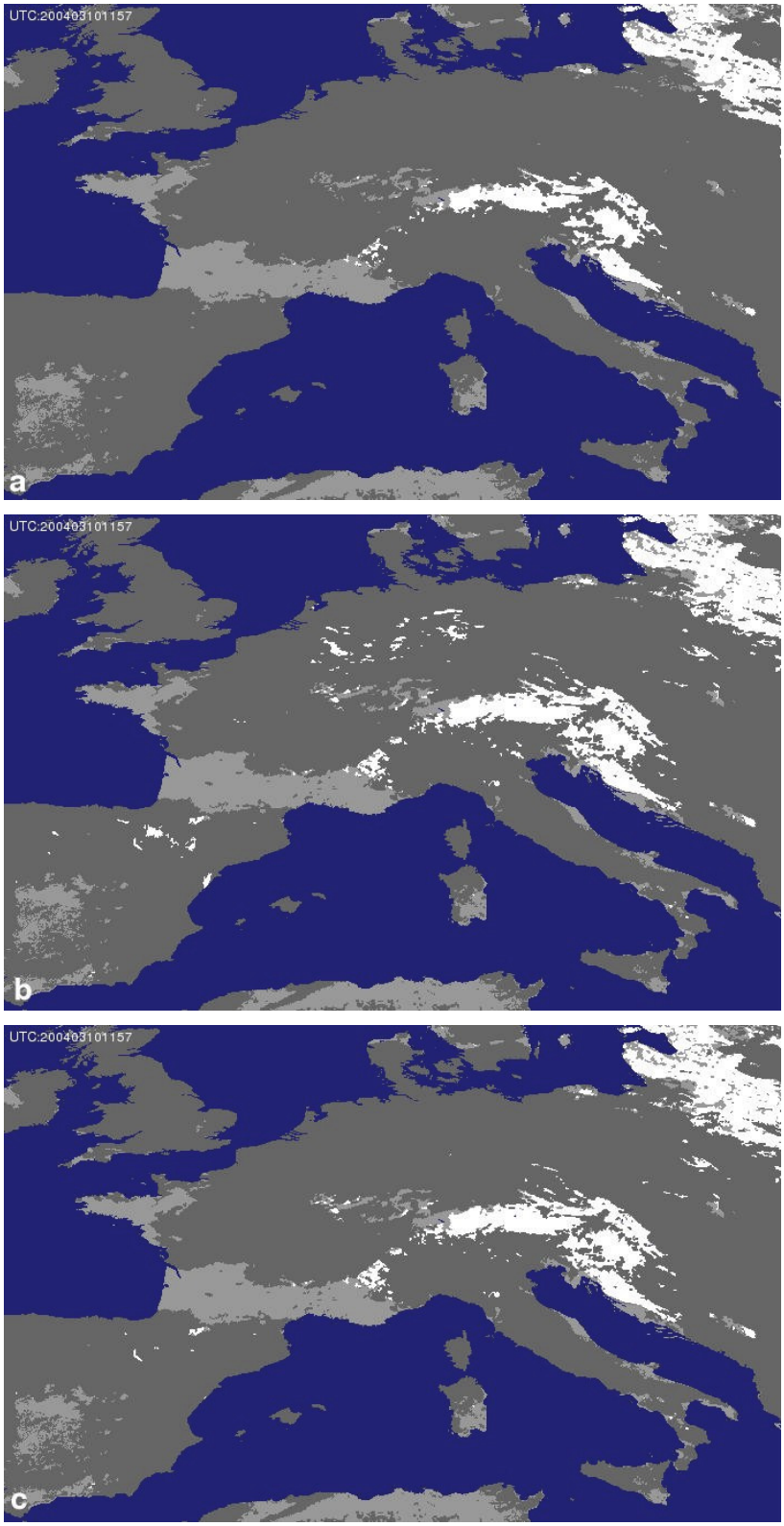

Figure 5: Instantaneous snow maps for March 10th, 2004, starting scan time 11:45. White pixels represent snow, dark grey pixels represent clouds and light grey pixels represent bare land. a) shows the result for the full classification method, including the temporal classification. For the other two maps, only the spectral classification was used, with $BT_{10.8,min} = 253 - 0.0063\,z$ *(b) and* $BT_{10.8,min} = 263 - 0.0063\,z$ *(c).*

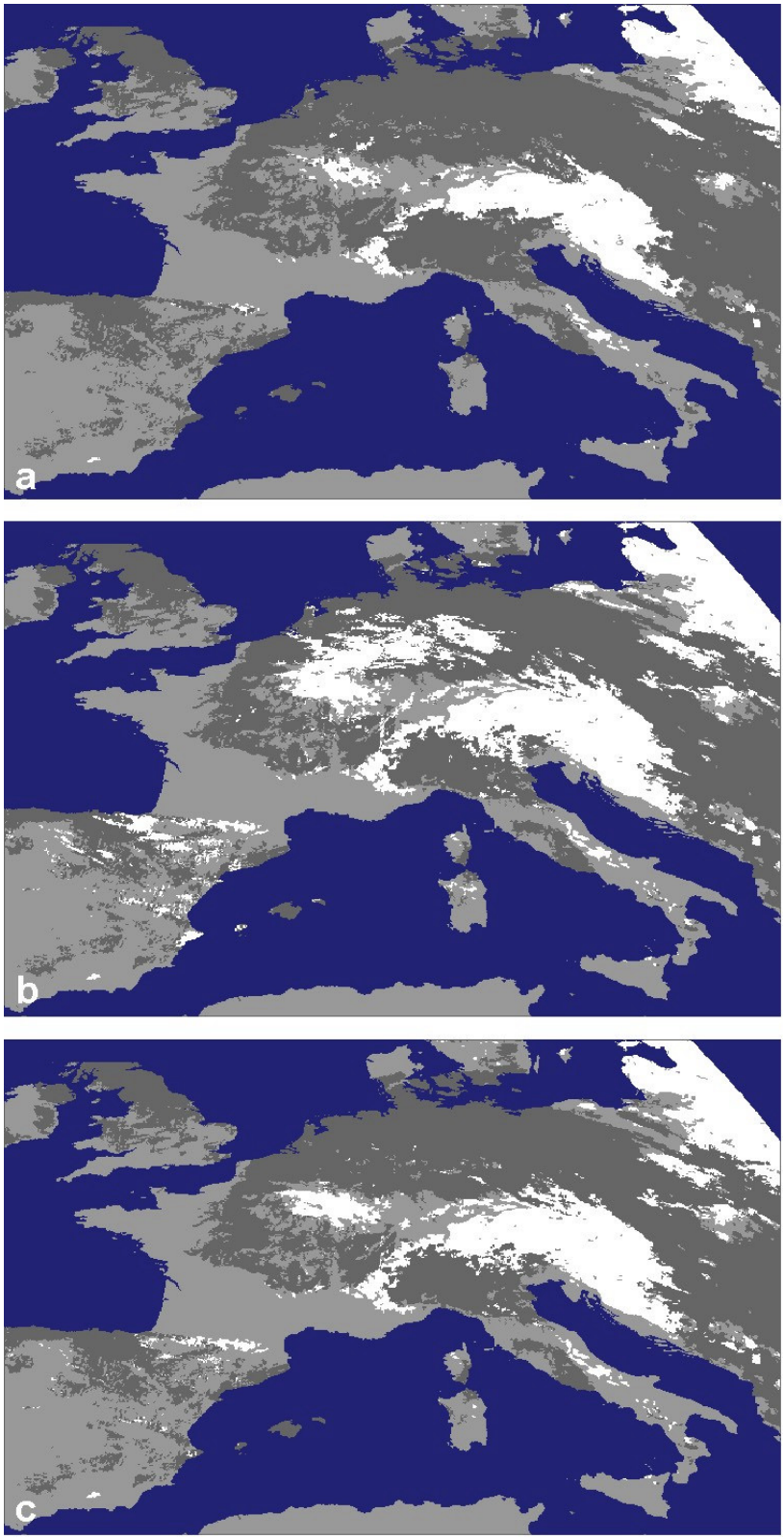

Figure 6: Same as Figure 5, but here composite snow maps for March 10th, 2004, are shown.

Optically thin ice clouds (cirrus) tend to be purple, whereas optically thick ice clouds resemble snow very closely (in red). Only the colour ranges of snow (red) and ice clouds (red/pink) overlap slightly. For qualitative discrimination between these two classes, animated time-series of the RGB combination are very helpful. Many clouds are clearly recognisable to the human eye on such animations because of their dynamic behaviour. Examples of animated time series are available on our project website (23).

Figure 4 shows that many of these ice clouds can be effectively masked with the temporal cloud masking algorithm. When the temporal differences in only one channel are used for cloud masking, many clouds are masked although numerous gaps remain (Figure 4a). Inclusion of the other features in the cloud mask strongly improves the result (Ffigure 4b). The classification result for the same image is displayed in Figure 5a. Visual inspection reveals that there are no clouds that are misclassified as snow. On the other hand, there are too many cloudy pixels over areas that are clearly snow-covered. This is caused by the temporal classification method which tends to overestimate the cloud-covered area. When we omit the temporal classification and only apply a spectral classification (Figure 5b), slightly more snow-covered pixels are classified correctly, e.g. over the Alps, but also a considerable number of cloudy pixels is now classified as snow. These pixels, noticeably occurring over Germany, northern Spain and northern Italy, correspond to ice clouds that are relatively warm. Raising the lower threshold for $BT_{10.8}$ by 10 K removes many of these pixels (Figure 5c), but some ice clouds, which obviously have a temperature close to the surface temperature, still remain over northern Spain and northern Italy. Raising the threshold further removes these pixels, but now non-cloudy pixels start being classified as clouds.

The large cloud-covered area which is visible in Figure 5 can be reduced by combining several successive snow maps into a composite map. The result for March 10th, 2004 is shown in Figure 6a. Now, much less pixels are cloud-covered and much more surface snow cover is visible. The composited maps for the two spectral classifications (i.e. without temporal classification) also display a strongly reduced cloudy area, but now the snow-covered area is over-estimated due to the misclassification of clouds (Figure 6b,c). The misclassified cloudy pixels, perhaps few in number in an individual snow map, often belong to clouds that travel considerable distances during a period of several hours. In the composite map, one and the same cloud can therefore cause a large area to be misclassified.

The composite snow map of Figure 6a can be validated qualitatively by comparing it with similar snow cover products. One such product is the MODIS daily composite snow cover product (5), which is available at the MODIS Land Quality Assessment Site (24). Figure 7 displays this daily composite for March 10th, 2004 as well as the Meteosat-8 snow map for the same day (equal to Figure 6a). The most noticeable difference from the Meteosat-8 snow map is the larger part of the surface that was not visible on this day due to cloud cover. This is mainly the case over southern and western Europe, where less snow-free surface is visible, and over central Europe, where less snow is visible. This difference is explained by the smaller number of available MODIS images as compared to the number of Meteosat-8 images. Another difference between the two snow maps is caused by the small isolated snow patches surrounded by clouds in the MODIS product, which do not occur in the Meteosat-8 product. An analysis of the animated time series of Meteosat-8 RGB's revealed that these pixels partly correspond to surface snow cover and partly to ice clouds. All of these pixels are classified as clouds by the temporal component of the Meteosat-8 algorithm, because these pixels or neighbouring cloudy pixels display temporal variability. Thus, the temporal classification of the METEOSAT-8 algorithm overestimates the amount of clouds, but by doing so it misses no ice clouds.

CONCLUSIONS

Spectral classification of single Meteosat-8 images separates snow and clouds reasonably well. Problems arise when optically thick clouds occur that contain ice crystals and that are relatively warm. Such clouds can have spectral characteristics similar to those of snow: a high visual reflectance, a low near-infrared reflectance and a relatively high brightness temperature. An alternative way to classify such clouds is to make use of their temporal context. We tested several classifiers that are based on the temporal difference and found that the separation between clear and cloudy regions improves as more temporal information is taken into account. The temporal algorithm slightly overestimates the number of cloudy pixels, but the pixels classified as cloud-free have a high reliability. The resulting snow map can therefore be considered conservative in the sense that the probability of rejecting a correct snow pixel (type I error) is larger than the probability of accepting a false snow pixel (type II error). Fortunately, the number of cloudy pixels can be strongly re-

duced by combining several instantaneous snow maps in one composite snow map. Also, for NWP models this conservatism is desirable, as a type I error has less severe consequences than a type II error. When the surface snow cover is obscured by clouds, the snow cover during the previous period or the modelled snow cover may be used, whereas erroneous snow cover will introduce errors in the NWP model computations.

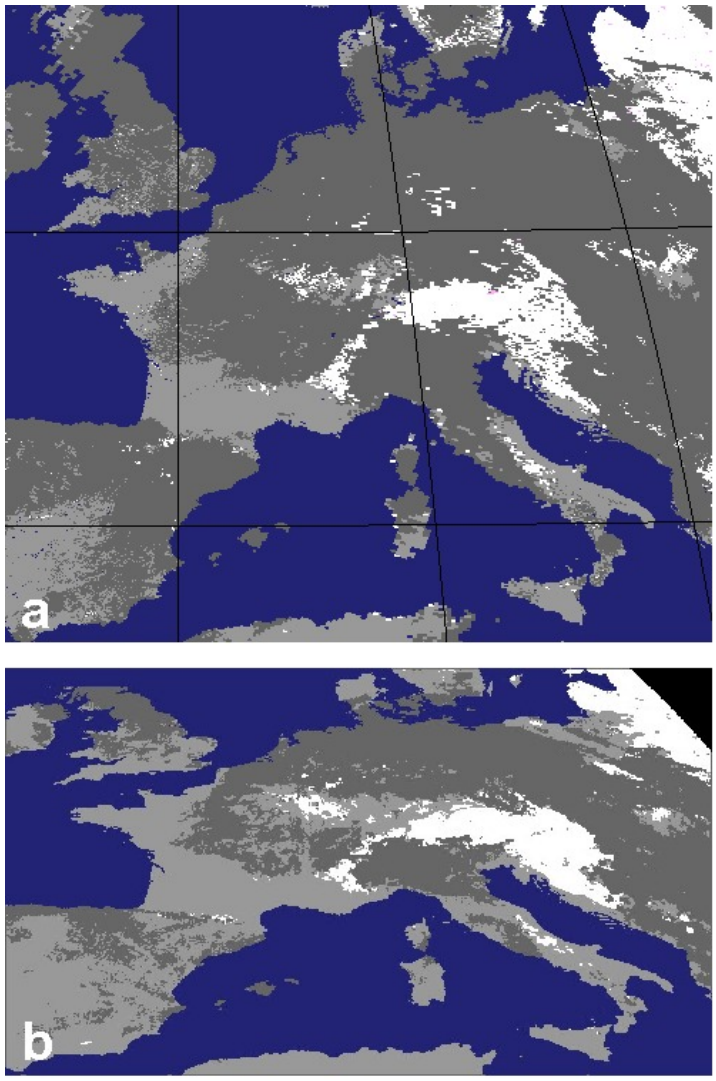

Figure 7: (a) MODIS composite snow map of central Europe for March 10th, 2004. White pixels represent snow, light grey pixels represent snow-free surface and dark grey pixels were not visible on this day. This image was obtained from the MODIS Land Quality Assessment Site (24). (b) Meteosat-8 snow map for the same day (equal to Figure 6a).

A first validation of the results has been performed by comparing them with the MODIS snow product and by visual inspection of animations of RGB combinations. We consider such a visual inspection a reliable way for qualitative validation, because the animations, in contrast to single images or RGB combinations, reveal the dynamic behaviour that many clouds display. A more elaborate quantitative validation will be performed in the near future with *in situ* snow observations and other satellite images (e.g. MODIS, MISR and MERIS). We will also use additional periods for testing and validation in order to see, how the algorithm performs under other meteorological conditions. Furthermore, the algorithm has room for several improvements such as corrections for atmospheric influence and anisotropy, inclusion of surface topography, detection of fractional instead of binary snow cover, and inclusion of quality flags.

ACKNOWLEDGEMENTS

We kindly thank two anonymous reviewers and the scientific editor Stefan Wunderle for their input. EUMETSAT provided the Meteosat-8 images and the SEVIRI Preprocessing Toolbox. Beat Rüedin helped with reading the images from tape and solved a number of hardware and software problems. We also would like to thank Jean-Marie Bettems, Igor Giunta, Jean Quiby and Hans Peter Roesli of MeteoSwiss for their input.

REFERENCES

1 Ebert E A, 1987. pattern recognition technique for distinguishing surface and cloud types in the polar regions. Journal of Climate and Applied Meteorology, 26: 1412-1427

2 Gesell G, 1989. An algorithm for snow and ice detection using AVHRR data. An extension to the APOLLO software package. International Journal of Remote Sensing, 10(4,5): 897-905

3 Allen R C Jr., P A Durkee & C H Wash, 1990. Snow/cloud discrimination with multispectral satellie measurements. Journal of Applied Meteorology, 29: 994-1004

4 Baum B A & Q Trepte, 1999. A grouped threshold approach for scene identification in AVHRR imagery. Journal of Atmospheric and Oceanic Technology, 16: 793-800

5 Hall D K, G A Riggs, V V Salomonson, N E DiGirolamo & K J Bayr, 2002. MODIS snow-cover products. Remote Sensing of Environment, 83: 181-194

6 Dozier J, 1989. Spectral signature of alpine snow cover from the Landsat Thematic Mapper. Remote Sensing of Environment, 28: 9-22

7 Logar A M, D E Lloyd, E M Corwin, M A Penaloza, R E Feind, T A Berendes, K-S Kuo & R M Welch, 1998. The ASTER Polar Cloud Mask. IEEE Transactions on Geosciences and Remote Sensing, 36(4): 1302-1312

8 Welch R M, D Berendes, T A Berendes, K-S Kuo & A M Logar, 1999. The ASTER polar cloud mask algorithm theoretical basis document. NASA EOS ASTER, ATBD-AST-13

9 Malcher P, D Floricioiu & H Rott, 2003. Snow mapping in alpine areas using medium resolution spectrometric sensors. In: Proceedings IEEE IGARSS03 (Toulouse), 4630 pp., vol. 4: 2835-2837

10 Romanov P, G Gutman & I Csiszar, 2000. Automated monitoring of snow cover over North America with multispectral satellite data. Journal of Applied Meteorology, 39: 1866-1880

11 Romanov P, D Tarpley, G Gutman & T Carroll, 2003. Mapping and monitoring of the snow cover fraction over North America. Journal of Geophysical Research, 108(D16): art. no. 8619

12 Le Gléau H, 2004. Software user manual of the SAFNWC/MSG: Scientific part for the PGE01-02-03 (EUMETSAT SAFNWC / Météo-France)

13 http://www.eumetsat.int/

14 Welch R M, S K Sengupta, A K Goroch, P Rabindra, N Rangaraj & M S Navar, 1992. Polar cloud and surface classification using AVHRR imagery: an intercomparison of methods. Journal of Applied Meteorology, 31: 405-420

15 Tovinkere V R, M A Penaloza, A Logar, J Lee, C Weger, T A Berendes & R M Welch, 1993. An intercomparison of artificial intelligence approaches for polar scene identification. Journal of Geophysical Research, 98(D3): 5001-5016

16 Govaerts Y M, S Wagner & M Clerici, 2004. SEVIRI Native Format pre-processing toolbox user's guide, issue SPT VERSION 2.2. Document No. EUM/OPS-MSG/TEN/03/0011 (EUMETSAT), 59 pp.

17 Govaerts Y M, A Arriaga & J Schmetz, 2001. Operational vicarious calibration of the MSG/SEVIRI solar channels. Advances in Space Research, 28: 21–30

18 Schmetz J, P Pili, S Tjemkes, D Just, J Kerkmann, S Rota & A Ratier, 2002. Supplement to An Introduction to Meteosat Second Generation (MSG). Seviri calibration. Bulletin of the American Meteorology Society, 83(7): 992-992

19 Riggs, G & D K Hall, 2002. Reduction of cloud obscuration in the MODIS snow data product. In: Proceedings of the 59th Eastern snow conference (Stowe, Vermont)

20 Hunt G E, 1973. Radiative properties of terrestrial clouds at visible and infra-red thermal window wavelengths. Quarterly Journal of the Royal Meteorology Society, 99: 346-369

21 Hall D K, G A Riggs & V V Salomonson, 1995. Development of methods for mapping global snow cover using moderate resolution imaging spectroradiometer data. Remote Sensing of Environment, 54: 127-140

22 Wu R, J A Weinman & R T Chin, 1985. Determination of rainfall rates from GOES satellite images by a pattern recognition technique. Journal of Atmospheric and Oceanic Technology, 2(3): 314-330

23 http://www.photogrammetry.ethz.ch/research/snow/index.html

24 http://landweb.nascom.nasa.gov/cgi-bin/browse/browse.cgi